Human RAD52 Captures and Holds DNA Strands, Increases DNA Flexibility, and Prevents Melting of Duplex DNA: Implications for DNA Recombination

Ineke Brouwer, Hongshan Zhang, Andrea Candelli, Davide Normanno, Erwin J G Peterman, Gijs J L Wuite, Mauro Modesti

Cell Reports

Report

Human RAD52 Captures and Holds DNA Strands, Increases DNA Flexibility, and Prevents Melting of Duplex DNA: Implications for DNA Recombination

Graphical Abstract

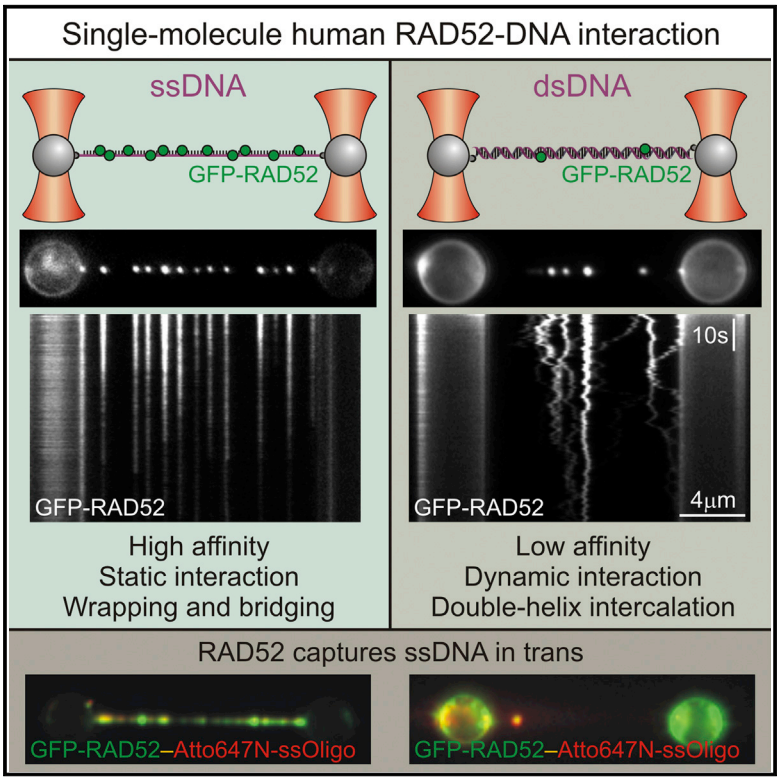

Highlights

- RAD52 binds ssDNA rapidly and tightly using wrapping and bridging modes
- RAD52 binding to dsDNA is slower, weaker, and often diffusive
- RAD52 changes dsDNA mechanics and intercalates into the double helix
- RAD52 prevents DNA melting by clamping DNA strands

Authors

Ineke Brouwer, Hongshan Zhang, Andrea Candelli, Davide Normanno, Erwin J.G. Peterman, Gijs J.L. Wuite, Mauro Modesti

Correspondence

e.j.g.peterman@vu.nl (E.J.G.P.), g.j.l.wuite@vu.nl (G.J.L.W.), mauro.modesti@inserm.fr (M.M.)

In Brief

Brouwer et al. show that human RAD52 swiftly and tightly wraps ssDNA around itself. With dsDNA, interactions are weaker and diffusive but drastically change DNA mechanics, suggesting double helix intercalation. DNA-bound RAD52 efficiently captures ssDNA in *trans*. These features seem favorable for strand annealing, clamping, and second-end capture.

Brouwer et al., 2017, Cell Reports *18*, 2845–2853
March 21, 2017
http://dx.doi.org/10.1016/j.celrep.2017.02.068

CellPress

Cell Reports
Report

Human RAD52 Captures and Holds DNA Strands, Increases DNA Flexibility, and Prevents Melting of Duplex DNA: Implications for DNA Recombination

Ineke Brouwer,[1,3] Hongshan Zhang,[2,3] Andrea Candelli,[1] Davide Normanno,[2] Erwin J.G. Peterman,[1,*] Gijs J.L. Wuite,[1,*] and Mauro Modesti[2,4,*]
[1]Department of Physics and Astronomy and LaserLab, Vrije Universiteit Amsterdam, 1081 HV Amsterdam, the Netherlands
[2]Cancer Research Center of Marseille, CNRS UMR7258, Inserm U1068, Institut Paoli-Calmettes, Aix-Marseille Université UM105, 13273 Marseille, France
[3]Co-first author
[4]Lead Contact
*Correspondence: e.j.g.peterman@vu.nl (E.J.G.P.), g.j.l.wuite@vu.nl (G.J.L.W.), mauro.modesti@inserm.fr (M.M.)
http://dx.doi.org/10.1016/j.celrep.2017.02.068

SUMMARY

Human RAD52 promotes annealing of complementary single-stranded DNA (ssDNA). In-depth knowledge of RAD52-DNA interaction is required to understand how its activity is integrated in DNA repair processes. Here, we visualize individual fluorescent RAD52 complexes interacting with single DNA molecules. The interaction with ssDNA is rapid, static, and tight, where ssDNA appears to wrap around RAD52 complexes that promote intra-molecular bridging. With double-stranded DNA (dsDNA), interaction is slower, weaker, and often diffusive. Interestingly, force spectroscopy experiments show that RAD52 alters the mechanics dsDNA by enhancing DNA flexibility and increasing DNA contour length, suggesting intercalation. RAD52 binding changes the nature of the overstretching transition of dsDNA and prevents DNA melting, which is advantageous for strand clamping during or after annealing. DNA-bound RAD52 is efficient at capturing ssDNA in *trans*. Together, these effects may help key steps in DNA repair, such as second-end capture during homologous recombination or strand annealing during RAD51-independent recombination reactions.

INTRODUCTION

Human RAD52 belongs to a ubiquitous class of proteins that helps to overcome the thermodynamic barrier required to anneal complementary DNA strands under biological conditions (Iyer et al., 2002; Sugiman-Marangos et al., 2016). In mammalian cells, RAD52 is important for repair of DNA double-strand breaks (DSBs) by the mutagenic RAD51-independent single-strand annealing pathway (SSA) (Bhargava et al., 2016; Morales et al., 2015; Stark et al., 2004). However, unlike its yeast ortholog, vertebrate RAD52 does not seem to be crucial for recombinational repair of DSBs via RAD51 (Rijkers et al., 1998; Yamaguchi-Iwai et al., 1998). The reason for this is that the RAD52 function to facilitate the loading of RAD51 on replication protein A (RPA)-coated single-stranded DNA (ssDNA) appears to have been taken over by breast cancer susceptibility protein 2 (BRCA2) (see commentary by Liu and Heyer, 2011 and references therein). However, the finding that RAD52 deficiencies are synthetically lethal with BRCA2 deficiencies suggests a functional redundancy between RAD52 and BRCA2 (Feng et al., 2011; Lok et al., 2013). These reports, together with the recent discovery that RAD52 is implicated in promoting DNA synthesis after replication stress (Bhowmick et al., 2016; Ciccia and Symington, 2016; Sotiriou et al., 2016) and in modulating antibody class-switch recombination (Zan et al., 2017), are fueling a regain of interest in studying the function of RAD52 for both fundamental and therapeutic purposes (Hanamshet et al., 2016).

RAD52 forms ring-shaped structures in vitro (Shinohara et al., 1998). In solution, full-length RAD52 forms stable heptameric rings with a large central channel, a structural organization reminiscent of hexameric DNA helicases (Stasiak et al., 2000). However, unlike hexameric DNA helicases, there is no evidence indicating that DNA passes through the channel of the RAD52 ring. In contrast, it has been proposed that ssDNA wraps around the outer surface of the RAD52 ring, interacting with an exposed positively charged groove (Singleton et al., 2002). Annealing of complementary ssDNA might then involve ssDNA wrapping and dynamic interactions between multiple RAD52 rings (Grimme et al., 2010; Rothenberg et al., 2008).

Here, we directly visualize and quantify the interaction of fluorescently labeled human RAD52 with individual ssDNA and double-stranded DNA (dsDNA) molecules using a single-molecule approach that combines optical trapping with microfluidics and fluorescence microscopy. We report intrinsic properties of RAD52-DNA interactions, including binding stoichiometry, diffusivity, and effect on DNA mechanics, and discuss the implications of our findings on the biological roles of RAD52.

RESULTS AND DISCUSSION

Experimental Approach

After expression in bacteria, human RAD52 tagged at the N terminus with EGFP (GFP-RAD52) was purified (Figure S1A) and tested in strand-annealing kinetic assays (details of experimental procedures can be found in Supplemental Experimental Procedures). We found no appreciable differences in activity compared to the untagged variant (Figures S1B and S1C), in agreement with previous studies where GFP-RAD52 fully rescued the synthetic lethality of BRCA2 RAD52 double-deficient cells (Feng et al., 2011; Lok et al., 2013).

To study the interaction of GFP-RAD52 with individual DNA molecules, we used a combination of optical trapping, fluorescence microscopy, and microfluidics (Brouwer et al., 2016; Heller et al., 2014a, 2014b). Using two independent optical traps, individual DNA molecules could be manipulated while simultaneously detecting the tension on the DNA. dsDNA molecules were biotinylated on the 3′ ends of both top and bottom DNA strands (Candelli et al., 2013) and were tethered to optically trapped streptavidin-coated polystyrene microspheres (Figure S1D). Single ssDNA tethers (Figure S1E) were generated by biotinylation of both the 5′ and 3′ ends of the top strand of a dsDNA molecule and subsequent detachment of the bottom strand by force-induced melting (Candelli et al., 2013). After incubation of the dsDNA and ssDNA constructs in a GFP-RAD52 solution, the DNA tethers were brought into a buffer channel where DNA-bound proteins could be visualized in the absence of fluid flow and fluorescent proteins in solution (Figures S1F and S1G). To facilitate in situ generation of ssDNA templates and DNA-protein complexes, our approach included laminar flow microfluidics, which allows fast exchange between buffers containing microspheres, DNA, protein-free, and protein solutions (Figures S1H and S1I).

GFP-RAD52 Binding to ssDNA Is Avid and Shortens ssDNA Contour Length

The affinity of RAD52 for ssDNA has been reported to be much higher than for dsDNA (Van Dyck et al., 1998). To quantitatively assess the affinity for ssDNA, single ssDNA molecules were (unless otherwise indicated) incubated at a tension of 10 pN in a buffer containing 1 nM of GFP-RAD52; 20 mM Tris-HCl (pH 7.6); 100 mM KCl; and either 1 mM Ca^{2+}, 1 mM Mg^{2+}, or no divalent cations. Protein complexes formation on the DNA was assessed from the fluorescence intensity (under constant continuous excitation with 500 ms exposure time/frame) immediately after transfer of the construct to a protein-free environment. We observed discrete fluorescent patches along the ssDNA constructs, with each patch corresponding to an oligomeric DNA-bound GFP-RAD52 complex. In the presence of Ca^{2+}, loading of GFP-RAD52 is remarkably fast: after 5 s incubation in 100 pM GFP-RAD52, significant amounts of fluorescent protein were bound to the ssDNA (Figure 1A, left panel). Under these conditions, the observed rate of patch formation was 35 ± 3 oligomers s^{-1} nM^{-1} (n = 43). In the presence of Mg^{2+}, a much lower rate of $(5 \pm 1)\cdot10^{-2}$ oligomers s^{-1} nM^{-1} (n = 11) was observed and loading of similar amounts of protein on ssDNA required a much longer incubation (100 s) at 10-fold higher GFP-RAD52 concentration (Figure 1A, middle panel). When no divalent cation was present, binding of GFP-RAD52 was even less efficient and the patch formation rate was $(1.2 \pm 0.5)\cdot10^{-2}$ oligomers s^{-1} nM^{-1} (n = 25; Figure 1A, right panel). Interactions appeared independent of DNA sequence (Figure S2A); most patches detected on ssDNA appeared static (see analysis of protein diffusion below); and within the (limited) observation time of our experiments (about 2 min), we did not observe dissociation of the GFP-RAD52 patches from the DNA, which implies a dissociation rate smaller than 0.008 s^{-1}. We thus show that GFP-RAD52 interacts efficiently and statically with ssDNA in a cation-dependent manner.

Next, we determined the stoichiometry of the DNA-bound complexes by quantifying the fluorescence intensity of the complexes and normalizing to that of an individual GFP (Figure S3). Stoichiometry distributions were typically very broad, ranging from one to several tens of GFP-RAD52 monomers per complex (Figure 1B). We found no evidence for the strict heptameric structure reported previously (blue dotted lines in Figure 1B; Stasiak et al., 2000). Heptamers, the dominant species in solution, may thus rearrange into different oligomeric complexes when the protein interacts with ssDNA. Nevertheless, further experiments are needed to directly observe this putative rearrangement and assess to what extent the deviation from the $7\cdot n$ distribution expected for heptamers and multiples of heptamers is caused by quenching of the EGFP fluorescence by homo-FRET or because of a dark, non-fluorescent fraction in the GFP-RAD52 preparations. In the presence of Ca^{2+}, the average patch size was significantly larger than in the presence of Mg^{2+} or without divalent cations (Figure 1C). Applying tension to the ssDNA substrate did not have a significant effect on the average number of patches (Figure S2B) and their size (Figure S2C). To further address how RAD52 interacts with ssDNA, we performed an experiment where a ssDNA construct was repeatedly incubated in the GFP-RAD52 channel, each incubation lasting 2 s. The position of the fluorescent patches was recorded and photobleached afterward. Subsequently, the recorded positions of the successive incubations were compared (Figure S2D; representative example out of eight experiments). The probability of detecting a fluorescent patch at the same position during successive incubations is in the order of $14\% \pm 4\%$ (SEM), indicating that the rates of initial patch formation and of patch growth are of the same order, unlike RAD51, which exhibits rate-limiting nucleation and a fast polymerization rate (Candelli et al., 2014).

We also studied the impact of GFP-RAD52 binding on the mechanical properties of ssDNA. To this end, we incubated ssDNA constructs in a buffer containing GFP-RAD52 at very low tension, allowing different segments of the ssDNA to interact with each other. Next, the constructs were brought into a protein-free buffer channel, where force-extension and force-relaxation curves were measured. In these curves, two clear effects were observed. In the extension curves (Figure 1D), rupture events were observed, where a large, abrupt increase in DNA extension was observed without an increase in force (orange arrows). The average increase in contour length for a single rupture event was 0.35 ± 0.02 μm (mean ± SEM;

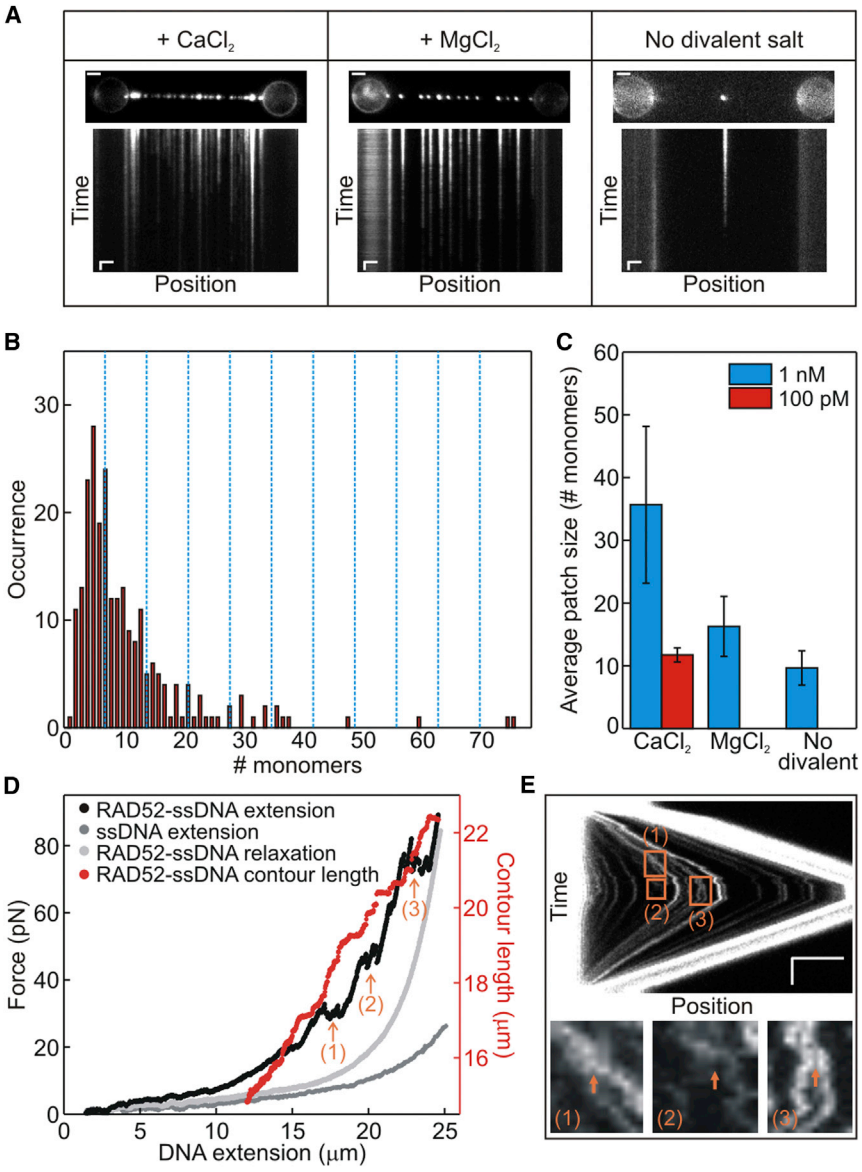

Figure 1. Binding of GFP-RAD52 to ssDNA

(A) Fluorescence images (top panels) and kymographs (bottom panels) of GFP-RAD52 on ssDNA in the presence of the indicated divalent cations. ssDNA molecules were held at 10 pN tension and incubated in a buffer containing 100 pM GFP-RAD52 for 5 s in the presence of $CaCl_2$ or 1 nM GFP-RAD52 for 100 s in the presence of $MgCl_2$ or in the absence of divalent cation. The scale bars represent 2 μm and 5 s.

(B) Size distribution of GFP-RAD52 oligomers bound to ssDNA, measured in $CaCl_2$ at 100 pM with an average of 11 ± 1 monomers (mean ± SEM; n = 238). Dashed blue lines indicate multiples of seven monomers. Similar distributions were obtained for all the conditions tested.

(C) Bar plot showing how the average patch size varies with varying divalent cations at 1 nM and 100 pM GFP-RAD52. At 100 pM, no binding was detected within our incubation times in the presence of Mg^{2+} or in the absence of divalent cation. The error bars represent statistical errors in the number of counts.

(D) Force-extension curves during successive extension and retraction of GFP-RAD52-ssDNA complexes formed by incubation of the ssDNA with 5 nM GFP-RAD52 in 30 mM KCl. Red trace shows the corresponding (calculated) contour length during the extension trace.

(E) (Top panel) Kymograph of the fluorescence signal corresponding to (D). (Bottom panel) Enlargement of the events indicated by (1), (2), and (3) shows clear ruptures of protein-protein bridges. The scale bars represent 5 μm and 10 s.

Figure S2E). The relaxation curves, on the other hand, showed no such ruptures and appeared smooth, but the ssDNA was significantly shorter than naked ssDNA. This shortening persists up to forces above 80 pN (Figure 1D). The rupture events could be attributed to tension-induced rupture of protein-protein bridges, as can be observed in the corresponding fluorescence kymographs (Figure 1E) or to the rupture of short stretches of dsDNA that were formed through RAD52-mediated annealing of partially complementary DNA segments. In addition, the shortening of the GFP-RAD52-ssDNA construct with respect to naked ssDNA can be attributed either to very strong (and thus unbroken) protein-protein bridges or to ssDNA that is wrapped around the protein complexes. Hence, this behavior is consistent with the proposal that ssDNA wrapping and ring-ring contacts might be involved in RAD52-promoted strand annealing (Grimme et al., 2010; Rothenberg et al., 2008).

GFP-RAD52 Binding Increases Flexibility and Contour Length of dsDNA and Prevents Melting

Although biochemical studies have mostly focused on the binding of RAD52 to ssDNA, there is also evidence for RAD52 interacting with dsDNA (Hengel et al., 2016; Van Dyck et al., 1998), despite the biological relevance of such interaction remaining subject of debate. To detect dsDNA binding, we worked at 20 nM GFP-RAD52 concentration; as reference, the RAD52 concentration in yeast is ~1 nM (Ghaemmaghami et al., 2003). Interestingly, RAD52 has a secondary DNA binding site that is important for dsDNA binding, likely regulated by phosphorylation, and required to introduce positive supercoiling in dsDNA upon RAD52 binding (Honda et al., 2011; Kagawa et al., 2008). Here, we used our single-molecule approach to directly observe the binding of GFP-RAD52 to dsDNA. As for the interaction with ssDNA, binding was dependent on the divalent cation present: GFP-RAD52 binds to dsDNA more readily in the presence of Ca^{2+} (average patch formation rate $[26 \pm 4] \cdot 10^{-3}$ oligomers s^{-1} nM^{-1} [n = 66]), than in the presence of Mg^{2+} ($[3.9 \pm 0.3] \cdot 10^{-3}$ oligomers s^{-1} nM^{-1} [n = 101]) or in the absence of divalent cations ($[2.9 \pm 0.5] \cdot 10^{-3}$ oligomers s^{-1} nM^{-1} [n = 38]; Figure 2A). From these numbers, it is clear that, in the presence

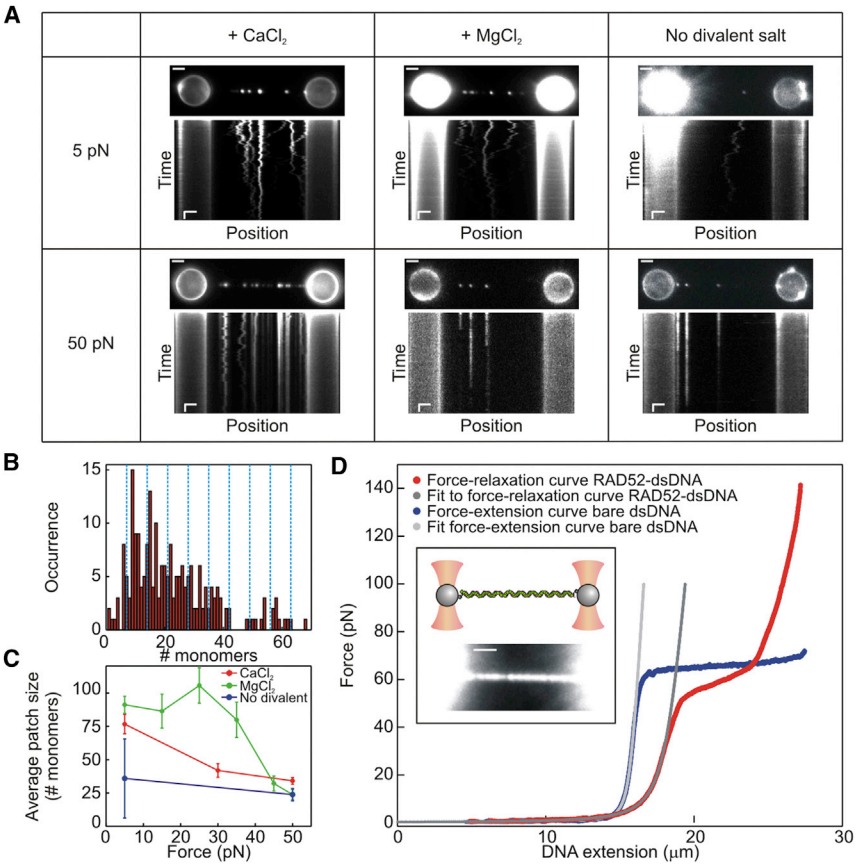

Figure 2. Binding of GFP-RAD52 to dsDNA

(A) Fluorescence images (top panels) and kymographs (bottom panels) of GFP-RAD52 on dsDNA in the presence of the indicated divalent cations and dsDNA template tensions. The dsDNA molecule was incubated in a channel containing 20 nM GFP-RAD52. Incubation times were 20 s for $CaCl_2$ at 5 pN, 30 s for $CaCl_2$ at 50 pN, 50 s for $MgCl_2$ at both forces and for no divalent cation at 50 pN, and 300 s for no divalent cation at 5 pN. As on ssDNA, most binding is observed in the presence of Ca^{2+}, slightly less binding is observed in presence of Mg^{2+}, and the lowest affinity is observed without divalent cation. GFP-RAD52 shows a dynamic behavior at low force, whereas it binds in a more static fashion at higher forces. The scale bars represent 2 μm and 5 s.

(B) Size distribution (n = 242) of GFP-RAD52 oligomers bound to dsDNA, average of 34 ± 3 monomers (mean ± SEM), measured at 20 nM GFP-RAD52, 50 pN tension, in the presence of $CaCl_2$. Dashed blue lines indicate multiples of seven monomers. Similar distributions were obtained for all the conditions tested.

(C) Relation between average patch size and DNA tension for the cationic conditions studied. As dsDNA tension is increased, the average patch size decreases by 4-fold in the 5–50 pN range. In addition, cationic conditions slightly influence the patch size. The error bars represent SEM.

(D) Mechanical properties of GFP-RAD52-dsDNA complexes determined by force-relaxation experiments (red curve). Up to 30 pN, the curve is well described by the eWLC model (dark gray). Compared to bare dsDNA (blue and light gray), a significant decrease in persistence length and a slight increase in contour length are observed (see Table 1). The inset shows the fluorescence image of the dsDNA, covered by more than 4,500 GFP-RAD52 proteins, recorded before the stretching cycle. The scale bar represents 2 μm.

of divalent ions, the affinity for dsDNA is one to three orders of magnitude lower compared to the affinity for ssDNA. Again, the interaction of GFP-RAD52 with dsDNA appeared not to depend on DNA sequence (Figure S2A), and dissociation was slower than photobleaching, as found for the interaction with ssDNA. Unlike GFP-RAD52 binding to ssDNA, which predominantly involved static complexes, binding to dsDNA involved both static and diffusive complexes (Figure 2A), depending on the cation and applied tension. Also, when measured in Ca^{2+} and at 50 pN, the average patch size on dsDNA did not depend on incubation time (Figure S4A), indicating that patch growth is not cooperative.

Stoichiometry distributions of complexes bound to dsDNA were even broader than for ssDNA (Figure 2B), and also for dsDNA, we did not discern a clear 7·n distribution reminiscent of heptameric complexes. Again, a dependence of the stoichiometry distributions on the divalent cation present was observed, as well as a significant dependence on the tension applied to the construct (Figure 2C). At lower DNA tensions, GFP-RAD52 oligomers were larger than at higher tensions. This observation is in contrast to the interaction with ssDNA, which did not show dramatic tension dependence. Most likely, this is due to structural changes of bare dsDNA upon application of tension, causing disruption of base pairing resulting in force-induced melting or other structural states that are more ssDNA-like where RAD52 would preferentially bind with a stoichiometry reminiscent of that observed for ssDNA (King et al., 2013). For ssDNA, such structural transitions do not occur. On both templates, the size of these complexes depends on the presence of Ca^{2+} and Mg^{2+}. Whereas the difference in the presence or absence of divalent cation can be explained by the shielding effect of their positive charges on the negatively charged phosphodiester backbone of DNA, the difference between Ca^{2+} and Mg^{2+} cannot be directly explained. Nevertheless, it is interesting to note here that Ca^{2+} greatly favors association kinetics of GFP-RAD52 with DNA. In light of previous studies that showed an important role of Ca^{2+} in the control of homologous recombination in human by affecting the ATPase activity of RAD51 (Bugreev and Mazin, 2004; Mazina and Mazin, 2004), our findings suggest that Ca^{2+} could have a much wider impact on DNA recombination transactions in human cells not only by stimulating RAD51-mediated strand exchange but also RAD52-mediated strand annealing.

Next, we investigated the effect of GFP-RAD52 binding on the mechanical properties of dsDNA using dsDNA constructs with a high coverage of GFP-RAD52. We observe smooth force-extension and relaxation curves (Figures 2D, S4B, and S4C) that did not show evidence for protein-protein bridges or DNA wrapping,

Table 1. GFP-RAD52-dsDNA Complexes as an Extensible Worm-like Chain

Conditions	Stretching Direction	Number of Experiments	L_p (nm)	L_c (μm)	S (pN)
GFP-RAD52-dsDNA	relaxation	8	5.5 ± 0.9	19.4 ± 0.4	(21 ± 7)·10^2
Naked dsDNA	extension	20	45 ± 2	15.96 ± 0.02	(18 ± 1)·10^2
Naked dsDNA	relaxation	18	47 ± 2	16.00 ± 0.02	(17 ± 1)·10^2

L_c, contour length; L_p, persistence length; S, stretch modulus. GFP-RAD52-dsDNA complexes and naked dsDNA were measured in a buffer containing $CaCl_2$. Errors: SEM.

in contrast to our observation for ssDNA. Individual force-extension curves show substantial variations (Figure S4B), likely due to DNA-bound protein complexes sticking nonspecifically to the microspheres. Relaxation curves, however, were reproducible and smooth (Figure S4C). For forces below 30 pN, these curves can be accurately described by the extensible-worm-like-chain (eWLC) model (Broekmans et al., 2016; Figure 2D). From the fit parameters in the presence and absence of GFP-RAD52 (Table 1), we deduce that GFP-RAD52 binding results in a (9 ± 1)-fold decrease of the persistence length and a (1.21 ± 0.03)-fold increase in contour length, whereas the stretch modulus is not affected. These properties suggest a possible binding mechanism of RAD52 to dsDNA through intercalation and opening of the double helix, which might be crucial for ATP-independent homology recognition and strand exchange by RAD52 (Bi et al., 2004; Reddy et al., 1997).

In the buffer conditions used, at forces above 30 pN, extension-relaxation cycles of bare dsDNA typically show a saw-tooth-like overstretching transition with a large hysteresis between the extension and relaxation curve (Figure S4D), signature of the force-induced melting of the DNA strands (Gross et al., 2011). For dsDNA coated with GFP-RAD52, the behavior is different: the curves remain smooth and the hysteresis between extension and relaxation curves is much smaller, indicating that force-induced melting of the DNA strands no longer occurs. The formation of ssDNA is thus prevented by GFP-RAD52, providing evidence for strand annealing and clamping activity for RAD52 reminiscent of the activity proposed for the bacteriophage λ Redβ ortholog, which is thought to clamp DNA strands together to secure homology recognition (Ander et al., 2015). RAD52 DNA-strand clamping might be an important property during second-end capture, for holding together annealed DNA repeats to allow processing of ssDNA flaps and DNA repair synthesis during the various types of homologous recombination after D-loop formation. Moreover, as was discovered in yeast, RAD52 could be part of a complex that tightly tethers the two ends of broken chromosomes, allowing them to withstand the pulling forces of the mitotic spindle (Lisby and Rothstein, 2004; Lobachev et al., 2004).

GFP-RAD52 Slides along dsDNA

When examining the binding of GFP-RAD52 to dsDNA (Figure 2A), we observed that, depending on the buffer and the tension applied on the construct, a fraction of the fluorescent patches moved along the DNA in a diffusive manner. To quantify this diffusive motion, we used custom-written tracking software to determine the trajectory of each individual fluorescent patch over time and used mean squared displacement (MSD) analysis to determine the one-dimensional diffusion coefficient of each patch (Figures S5A–S5D). Then, we applied a threshold of 583 nm^2/s (the minimal detectable diffusion coefficient in our experimental conditions; see Supplemental Experimental Procedures) to determine whether the complex was static or diffusive. For each tension and buffer condition studied, we generated the distribution of above-threshold diffusion coefficients (Figure 3A) and used two parameters to quantify the diffusive behavior: the average diffusion coefficient (calculated based on only the diffusive particles) and the diffusive fraction (the fraction of particles that diffused). Diffusion was most prominent at forces below 15 pN, where almost 100% of the particles were mobile. Both the average diffusion coefficient (Figure 3B) and the diffusive fraction (Figure 3C) decreased with increasing tension. The transition between static and diffusive behavior is reversible: when the force is increased, particles switch from a diffusive to a static state, and when the force is decreased again, particles may switch back to the diffusive mode (Figure 3D). Yet, no dependence of the diffusion coefficient on the nature of the divalent cation was observed (Figure 3E), and the diffusive fraction also did not change accordingly (Figure S5E). Finally, our data show no strong correlation between the diffusion coefficient and the size of the fluorescent patch (Figure 3F), indicating that diffusion is not limited by the drag force acting on the protein complex. A quantitative analysis revealed that RAD52 complexes also diffuse on ssDNA, albeit with smaller diffusion coefficients and diffusive fractions than on dsDNA and in a manner independent of the tension applied on the ssDNA construct (Figures S5F and S5G). In total, 25% ± 3% of the complexes bound to ssDNA showed diffusive behavior and the average diffusion coefficient was roughly 50-fold smaller for particles diffusing on ssDNA than on dsDNA (Figure 3E). From these data, we conclude that GFP-RAD52 can interact with DNA in either static or diffusive binding modes. The diffusive binding mode is predominantly observed on dsDNA and is slowed down when tension is applied on the dsDNA, which favors immobilization of RAD52 complexes by intercalation in the double helix (Figure 3G, top panel). This diffusive binding mechanism suggests a role for RAD52 in a diffusive search mechanism for localizing DNA structural intermediates, such as ssDNA-dsDNA interfaces.

DNA-Bound GFP-RAD52 Captures ssDNA in *trans*

Given the involvement of RAD52 in second-end capture during homologous recombination (McIlwraith and West, 2008; Nimonkar et al., 2009; Shi et al., 2009), we explored its ability to capture DNA in *trans*. GFP-RAD52 was first bound to dsDNA or to ssDNA, and the constructs were subsequently exposed to a solution of 60-mer ssDNA oligonucleotides fluorescently end

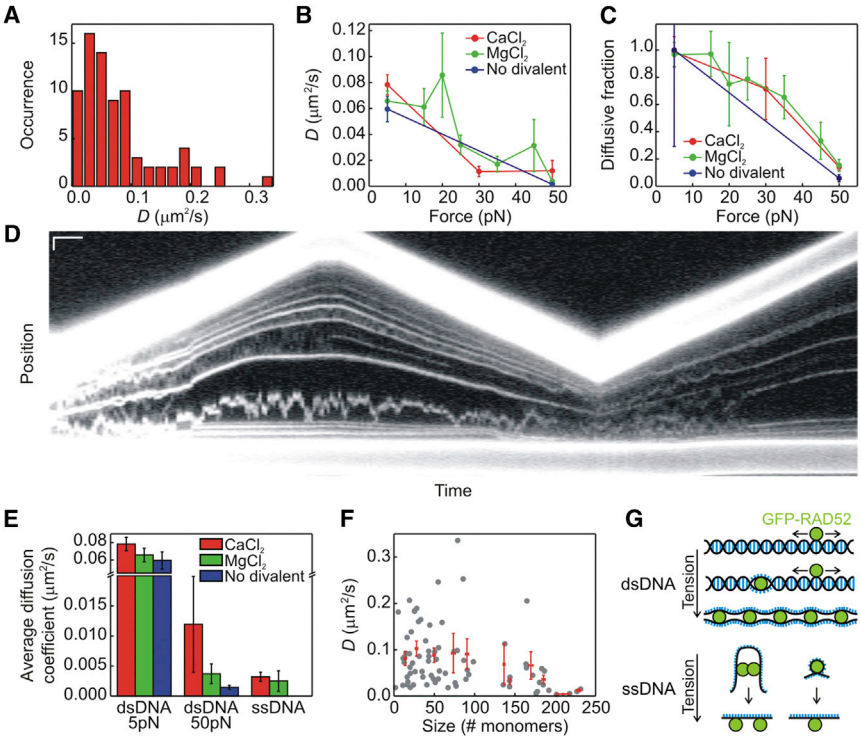

Figure 3. GFP-RAD52 Can Diffuse along DNA

(A) Histogram (n = 77) of the diffusion coefficients of the diffusive GFP-RAD52 complexes along dsDNA, measured in 20 nM GFP-RAD52 at 5 pN and in the presence of $CaCl_2$.

(B) Relation between average diffusion coefficient and dsDNA tension. A clear ~8-fold decrease is observed as the tension on the dsDNA molecule increases. The error bars represent SEM.

(C) The fraction of complexes that are mobile decreases with increasing tension. At low force, virtually all complexes show diffusive behavior, whereas at high tension, only a small fraction of complexes is mobile. The error bars represent statistical errors in the number of counts.

(D) Kymograph recorded during successive extension-relaxation cycles of a GFP-RAD52-dsDNA complex showing a clear force dependence of the diffusion: at low force, most complexes diffuse. When the force is increased, complexes switch to a static binding mode. When the force is decreased, complexes may switch back to diffusive behavior. Intensity is scaled logarithmically. The scale bars represent 2 μm and 5 s.

(E) Bar plot of the average diffusion coefficient for different divalent cations, forces, and DNA substrates. Diffusion is fastest in the presence of Ca^{2+}, slower in presence of Mg^{2+}, and slowest in the absence of divalent cations. The error bars represent SEM.

(F) Relation between diffusion coefficient and patch size, measured on dsDNA with a tension of 5 pN in the presence of Ca^{2+}. Grey dataset shows all individual data points, and red dataset shows the average diffusion coefficient of 20 consecutive data points of increasing complex size. The error bars represent SEM.

(G) Schematic summarizing the interaction of RAD52 with DNA. GFP-RAD52 interacts with dsDNA in a diffusive mode at low tension (1–5 pN; top). As the applied tension is increased, diffusion halts as GFP-RAD52 complexes intercalate the double helix. At high tension (>50 pN), GFP-RAD52 tightly clamps the DNA strands. The process is reversible, as GFP-RAD52 complexes resume diffusion when the applied tension is brought back to 5 pN. GFP-RAD52 binding to ssDNA is rapid, stable, and static, consisting of a combination of wrapping and bridging modes (bottom).

labeled with Atto647N. GFP-RAD52 bound to dsDNA exhibits a remarkably efficient ability to capture the ssDNA oligonucleotide in *trans* (Figure 4A). All out of 27 individual GFP-RAD52 fluorescent patches (green) observed on six independent dsDNA molecules held at 50 pN captured at least one ssDNA oligo (red). Under the same conditions, no Atto647N signal was detected on constructs that were not incubated with GFP-RAD52 (Figure 4B). Next, we performed similar experiments on ssDNA constructs held at 5 pN (Figure 4C). Again, analysis of six independent molecules pre-incubated with GFP-RAD52 showed detection of Atto647N signal co-localizing with the GFP-RAD52 patches. Control experiments with ssDNA constructs not pre-incubated with GFP-RAD52 revealed that the oligonucleotides bind to naked ssDNA to a much lesser extent than in the presence of GFP-RAD52 (Figure 4D). We conclude that DNA-bound GFP-RAD52 is efficient at capturing ssDNA from solution, reminiscent of its role in second-end capture.

Conclusions

We have provided a quantitative assessment of the interaction of human RAD52 with DNA, suggesting properties important for its physiological roles as summarized in Figure 3G. While interacting tightly with ssDNA through a combination of wrapping and bridging, RAD52 complexes bound to dsDNA profoundly affect dsDNA mechanics and can diffuse in a tension-dependent way along dsDNA. The substantial decrease in persistence length and slight increase in contour length observed upon RAD52 binding indicate that RAD52 binding increases dsDNA flexibility probably by destabilizing and intercalating into duplex DNA. Our findings suggest that the way by which RAD52 promotes strand exchange in vitro is not by a strand-invasion mechanism like the RAD51 or RecA nucleoprotein filament but rather results from the ability of RAD52 to change dsDNA structure, intercalating in the helix to make the bases available for pairing. Consistent with our model, it was previously observed that increasing the fractional A·T content of DNA increases the yields of in vitro strand exchange reactions by RAD52, likely because it would be easier for RAD52 to intercalate in A·T regions (Bi et al., 2004; Kumar and Gupta, 2004). Also, the overstretching behavior of dsDNA is profoundly altered in the presence of RAD52, suggesting that RAD52 prevents force-induced melting and thus providing evidence for strand-clamping activity. The methodology and findings reported here can now be used in future experiments to extend this analysis by studying how RAD52 interacts with RPA, a pivotal ssDNA-binding protein. Indeed, RAD52 will need to deal with RPA-coated ssDNA in the physiological context, and its direct physical and functional interaction with RPA appears to be essential for homologous recombination in yeast and mammalian cells, especially when long ssDNA substrates need to be processed (Jackson et al., 2002; Park et al., 1996; Sugiyama et al., 1998).

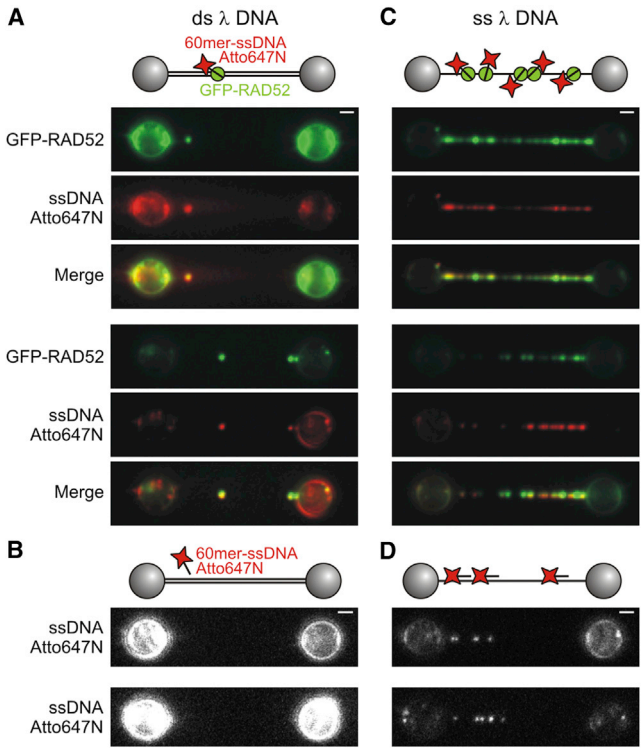

Figure 4. GFP-RAD52 Captures ssDNA in *trans*

(A) Two representative experiments showing ssDNA capture by GFP-RAD52 bound to dsDNA (n = 6). A dsDNA construct held at 50 pN was first incubated in a channel containing 50 nM GFP-RAD52 in the presence of Ca^{2+} for 30 s and then moved into a protein-free buffer channel to detect the binding positions of GFP-RAD52 (green). Next, the construct was incubated in a channel containing 10 nM Atto647N-labeled ssDNA Oligo for 30 s and subsequently moved to the observation channel to detect the binding positions of the oligo (red). Both signals were merged to detect where colocalization (yellow) has occurred.

(B) Two representative control experiments as in (A) but without GFP-RAD52.

(C) Two representative experiments showing ssDNA capture by GFP-RAD52 bound to ssDNA (n = 6). A ssDNA construct held at 5 pN was first incubated in a channel containing 5 nM GFP-RAD52 in the presence of Ca^{2+} for 30 s and then moved into a protein-free buffer channel to detect the binding positions of GFP-RAD52 (green). Next, the construct was incubated in a channel containing 10 nM Atto647N-labeled ssDNA Oligo for 30 s and subsequently moved to the observation channel to detect the binding of the oligo (red). Both signals were merged to detect where colocalization (yellow) has occurred.

(D) Two representative control experiments as in (C) but without GFP-RAD52. The scale bars represent 2 μm.

Further, the activities of BRCA2 could be similarly analyzed and directly compared to the ones of RAD52 to explore possible functional redundancies between the two proteins suggested by studies of the *Ustilago maydis* orthologs (Mazloum et al., 2007).

EXPERIMENTAL PROCEDURES

Expanded methods and details about proteins and DNA substrates and annealing and ssDNA oligo capture assays are provided in Supplemental Experimental Procedures.

Single-Molecule Experiments

Single-molecule experiments have been executed using a custom-build instrument (Gross et al., 2010) integrating optical trapping, wide-field fluorescence microscopy, and microfluidics. Beads and DNA catching were done in PBS buffer (pH 7.3–7.5). DNA melting for generation of ssDNA templates was performed in 20 mM Tris-HCl (pH 7.6). Protein, imaging, and ssDNA oligo buffer consisted of 20 mM Tris-HCl (pH 7.6); 100 mM KCl; and either 1 mM $MgCl_2$, 1 mM $CaCl_2$, or no divalent cations.

Quantification of Fluorescence Intensity

The stoichiometry of the DNA-bound GFP-RAD52 complexes was inferred from the number of GFP molecules in each fluorescent patch, calculated dividing the initial fluorescence intensity of the patch by the average intensity of a single GFP. We used a step-fitting algorithm (Kerssemakers et al., 2006) to extract the intensity of single GFPs from photo-bleaching traces (Figure S3A) of individual patches. The average GFP intensity was obtained from a Lorentzian fit to the histogram of step intensities (Figure S3B).

Quantification of Protein Diffusion

Diffusion was analyzed tracking GFP-RAD52 complexes for a large number of frames (on average 29 ± 2 s) and quantified using 1D MSD analysis (Heller et al., 2014b). Diffusion coefficients were calculated by linear fit to the first five points of the MSD curves (Figure S5D).

Statistical Analysis

Data are presented as mean ± SEM, and histograms show statistical errors in the number of counts. Data and images have been analyzed using custom-written LabView routines.

SUPPLEMENTAL INFORMATION

Supplemental Information includes Supplemental Experimental Procedures and five figures and can be found with this article online at http://dx.doi.org/10.1016/j.celrep.2017.02.068.

AUTHOR CONTRIBUTIONS

Conceptualization, M.M., I.B., A.C., and G.J.L.W.; Investigation, I.B., H.Z., and D.N.; Writing – Original Draft, I.B. and H.Z.; Writing – Review & Editing, I.B., H.Z., D.N., A.C., G.J.L.W., E.J.G.P., and M.M.; Funding Acquisition, G.J.L.W., E.J.G.P., and M.M.; Supervision, G.J.L.W., E.J.G.P., and M.M.

ACKNOWLEDGMENTS

We thank Claire Wyman, Bertrand Llorente, and Murray Junop for critical reading of the manuscript. This work was supported by the French National Research Agency (project RADORDER ANR-10-BLAN-1521; to M.M.), the ARC Foundation for Cancer Research (to M.M.), the A*MIDEX project (no. ANR-11-IDEX-0001-02) for the «Investissements d'Avenir» French Government program (to M.M.), funding from LASERLAB-EUROPE (grant agreement no. 284464; EC's Seventh Framework Programme; to M.M.), a fellowship from the Collège of Aix-Marseille Université (to H.Z.), a VICI grant of the Nederlandse Organisatie voor Wetenschappelijk Onderzoek (to G.J.L.W.), and a European Research Council starting grant (no. 260849-PhysGene; to G.J.L.W.).

Received: October 20, 2016
Revised: January 20, 2017
Accepted: February 21, 2017
Published: March 21, 2017

REFERENCES

Ander, M., Subramaniam, S., Fahmy, K., Stewart, A.F., and Schäffer, E. (2015). A single-strand annealing protein clamps DNA to detect and secure homology. PLoS Biol. *13*, e1002213.

Bhargava, R., Onyango, D.O., and Stark, J.M. (2016). Regulation of single-strand annealing and its role in genome maintenance. Trends Genet. *32*, 566–575.

Bhowmick, R., Minocherhomji, S., and Hickson, I.D. (2016). RAD52 facilitates mitotic DNA synthesis following replication stress. Mol. Cell *64*, 1117–1126.

Bi, B., Rybalchenko, N., Golub, E.I., and Radding, C.M. (2004). Human and yeast Rad52 proteins promote DNA strand exchange. Proc. Natl. Acad. Sci. USA *101*, 9568–9572.

Broekmans, O.D., King, G.A., Stephens, G.J., and Wuite, G.J.L. (2016). DNA twist stability changes with magnesium(2+) concentration. Phys. Rev. Lett. *116*, 258102.

Brouwer, I., Sitters, G., Candelli, A., Heerema, S.J., Heller, I., de Melo, A.J., Zhang, H., Normanno, D., Modesti, M., Peterman, E.J., et al. (2016). Sliding sleeves of XRCC4-XLF bridge DNA and connect fragments of broken DNA. Nature *535*, 566–569.

Bugreev, D.V., and Mazin, A.V. (2004). Ca^{2+} activates human homologous recombination protein Rad51 by modulating its ATPase activity. Proc. Natl. Acad. Sci. USA *101*, 9988–9993.

Candelli, A., Hoekstra, T.P., Farge, G., Gross, P., Peterman, E.J.G., and Wuite, G.J.L. (2013). A toolbox for generating single-stranded DNA in optical tweezers experiments. Biopolymers *99*, 611–620.

Candelli, A., Holthausen, J.T., Depken, M., Brouwer, I., Franker, M.A.M., Marchetti, M., Heller, I., Bernard, S., Garcin, E.B., Modesti, M., et al. (2014). Visualization and quantification of nascent RAD51 filament formation at single-monomer resolution. Proc. Natl. Acad. Sci. USA *111*, 15090–15095.

Ciccia, A., and Symington, L.S. (2016). Stressing out about RAD52. Mol. Cell *64*, 1017–1019.

Feng, Z., Scott, S.P., Bussen, W., Sharma, G.G., Guo, G., Pandita, T.K., and Powell, S.N. (2011). Rad52 inactivation is synthetically lethal with BRCA2 deficiency. Proc. Natl. Acad. Sci. USA *108*, 686–691.

Ghaemmaghami, S., Huh, W.-K., Bower, K., Howson, R.W., Belle, A., Dephoure, N., O'Shea, E.K., and Weissman, J.S. (2003). Global analysis of protein expression in yeast. Nature *425*, 737–741.

Grimme, J.M., Honda, M., Wright, R., Okuno, Y., Rothenberg, E., Mazin, A.V., Ha, T., and Spies, M. (2010). Human Rad52 binds and wraps single-stranded DNA and mediates annealing via two hRad52-ssDNA complexes. Nucleic Acids Res. *38*, 2917–2930.

Gross, P., Farge, G., Peterman, E.J.G., and Wuite, G.J.L. (2010). Combining optical tweezers, single-molecule fluorescence microscopy, and microfluidics for studies of DNA-protein interactions. Methods Enzymol. *475*, 427–453.

Gross, P., Laurens, N., Oddershede, L.B., Bockelmann, U., Peterman, E.J.G., and Wuite, G.J.L. (2011). Quantifying how DNA stretches, melts and changes twist under tension. Nat. Phys. *7*, 731–736.

Hanamshet, K., Mazina, O.M., and Mazin, A.V. (2016). Reappearance from obscurity: mammalian Rad52 in homologous recombination. Genes (Basel) *7*, 63.

Heller, I., Hoekstra, T.P., King, G.A., Peterman, E.J.G., and Wuite, G.J.L. (2014a). Optical tweezers analysis of DNA-protein complexes. Chem. Rev. *114*, 3087–3119.

Heller, I., Sitters, G., Broekmans, O.D., Biebricher, A.S., Wuite, G.J.L., and Peterman, E.J.G. (2014b). Mobility analysis of super-resolved proteins on optically stretched DNA: comparing imaging techniques and parameters. ChemPhysChem *15*, 727–733.

Hengel, S.R., Malacaria, E., Folly da Silva Constantino, L., Bain, F.E., Diaz, A., Koch, B.G., Yu, L., Wu, M., Pichierri, P., Spies, M.A., and Spies, M. (2016). Small-molecule inhibitors identify the RAD52-ssDNA interaction as critical for recovery from replication stress and for survival of BRCA2 deficient cells. eLife *5*, e14740.

Honda, M., Okuno, Y., Yoo, J., Ha, T., and Spies, M. (2011). Tyrosine phosphorylation enhances RAD52-mediated annealing by modulating its DNA binding. EMBO J. *30*, 3368–3382.

Iyer, L.M., Koonin, E.V., and Aravind, L. (2002). Classification and evolutionary history of the single-strand annealing proteins, RecT, Redbeta, ERF and RAD52. BMC Genomics *3*, 8.

Jackson, D., Dhar, K., Wahl, J.K., Wold, M.S., and Borgstahl, G.E.O. (2002). Analysis of the human replication protein A:Rad52 complex: evidence for crosstalk between RPA32, RPA70, Rad52 and DNA. J. Mol. Biol. *321*, 133–148.

Kagawa, W., Kagawa, A., Saito, K., Ikawa, S., Shibata, T., Kurumizaka, H., and Yokoyama, S. (2008). Identification of a second DNA binding site in the human Rad52 protein. J. Biol. Chem. *283*, 24264–24273.

Kerssemakers, J.W.J., Munteanu, E.L., Laan, L., Noetzel, T.L., Janson, M.E., and Dogterom, M. (2006). Assembly dynamics of microtubules at molecular resolution. Nature *442*, 709–712.

King, G.A., Gross, P., Bockelmann, U., Modesti, M., Wuite, G.J.L., and Peterman, E.J.G. (2013). Revealing the competition between peeled ssDNA, melting bubbles, and S-DNA during DNA overstretching using fluorescence microscopy. Proc. Natl. Acad. Sci. USA *110*, 3859–3864.

Kumar, J.K., and Gupta, R.C. (2004). Strand exchange activity of human recombination protein Rad52. Proc. Natl. Acad. Sci. USA *101*, 9562–9567.

Lisby, M., and Rothstein, R. (2004). DNA repair: keeping it together. Curr. Biol. *14*, R994–R996.

Liu, J., and Heyer, W.-D. (2011). Who's who in human recombination: BRCA2 and RAD52. Proc. Natl. Acad. Sci. USA *108*, 441–442.

Lobachev, K., Vitriol, E., Stemple, J., Resnick, M.A., and Bloom, K. (2004). Chromosome fragmentation after induction of a double-strand break is an active process prevented by the RMX repair complex. Curr. Biol. *14*, 2107–2112.

Lok, B.H., Carley, A.C., Tchang, B., and Powell, S.N. (2013). RAD52 inactivation is synthetically lethal with deficiencies in BRCA1 and PALB2 in addition to BRCA2 through RAD51-mediated homologous recombination. Oncogene *32*, 3552–3558.

Mazina, O.M., and Mazin, A.V. (2004). Human Rad54 protein stimulates DNA strand exchange activity of hRad51 protein in the presence of Ca^{2+}. J. Biol. Chem. *279*, 52042–52051.

Mazloum, N., Zhou, Q., and Holloman, W.K. (2007). DNA binding, annealing, and strand exchange activities of Brh2 protein from *Ustilago maydis*. Biochemistry *46*, 7163–7173.

McIlwraith, M.J., and West, S.C. (2008). DNA repair synthesis facilitates RAD52-mediated second-end capture during DSB repair. Mol. Cell *29*, 510–516.

Morales, M.E., White, T.B., Streva, V.A., DeFreece, C.B., Hedges, D.J., and Deininger, P.L. (2015). The contribution of alu elements to mutagenic DNA double-strand break repair. PLoS Genet. *11*, e1005016.

Nimonkar, A.V., Sica, R.A., and Kowalczykowski, S.C. (2009). Rad52 promotes second-end DNA capture in double-stranded break repair to form complement-stabilized joint molecules. Proc. Natl. Acad. Sci. USA *106*, 3077–3082.

Park, M.S., Ludwig, D.L., Stigger, E., and Lee, S.H. (1996). Physical interaction between human RAD52 and RPA is required for homologous recombination in mammalian cells. J. Biol. Chem. *271*, 18996–19000.

Reddy, G., Golub, E.I., and Radding, C.M. (1997). Human Rad52 protein promotes single-strand DNA annealing followed by branch migration. Mutat. Res. *377*, 53–59.

Rijkers, T., Van Den Ouweland, J., Morolli, B., Rolink, A.G., Baarends, W.M., Van Sloun, P.P., Lohman, P.H., and Pastink, A. (1998). Targeted inactivation of mouse RAD52 reduces homologous recombination but not resistance to ionizing radiation. Mol. Cell. Biol. *18*, 6423–6429.

Rothenberg, E., Grimme, J.M., Spies, M., and Ha, T. (2008). Human Rad52-mediated homology search and annealing occurs by continuous interactions between overlapping nucleoprotein complexes. Proc. Natl. Acad. Sci. USA *105*, 20274–20279.

Shi, I., Hallwyl, S.C.L., Seong, C., Mortensen, U., Rothstein, R., and Sung, P. (2009). Role of the Rad52 amino-terminal DNA binding activity in DNA strand capture in homologous recombination. J. Biol. Chem. *284*, 33275–33284.

Shinohara, A., Shinohara, M., Ohta, T., Matsuda, S., and Ogawa, T. (1998). Rad52 forms ring structures and co-operates with RPA in single-strand DNA annealing. Genes Cells *3*, 145–156.

Singleton, M.R., Wentzell, L.M., Liu, Y., West, S.C., and Wigley, D.B. (2002). Structure of the single-strand annealing domain of human RAD52 protein. Proc. Natl. Acad. Sci. USA *99*, 13492–13497.

Sotiriou, S.K., Kamileri, I., Lugli, N., Evangelou, K., Da-Ré, C., Huber, F., Padayachy, L., Tardy, S., Nicati, N.L., Barriot, S., et al. (2016). Mammalian RAD52 functions in break-induced replication repair of collapsed DNA replication forks. Mol. Cell *64*, 1127–1134.

Stark, J.M., Pierce, A.J., Oh, J., Pastink, A., and Jasin, M. (2004). Genetic steps of mammalian homologous repair with distinct mutagenic consequences. Mol. Cell. Biol. *24*, 9305–9316.

Stasiak, A.Z., Larquet, E., Stasiak, A., Müller, S., Engel, A., Van Dyck, E., West, S.C., and Egelman, E.H. (2000). The human Rad52 protein exists as a heptameric ring. Curr. Biol. *10*, 337–340.

Sugiman-Marangos, S.N., Weiss, Y.M., and Junop, M.S. (2016). Mechanism for accurate, protein-assisted DNA annealing by *Deinococcus radiodurans* DdrB. Proc. Natl. Acad. Sci. USA *113*, 4308–4313.

Sugiyama, T., New, J.H., and Kowalczykowski, S.C. (1998). DNA annealing by RAD52 protein is stimulated by specific interaction with the complex of replication protein A and single-stranded DNA. Proc. Natl. Acad. Sci. USA *95*, 6049–6054.

Van Dyck, E., Hajibagheri, N.M., Stasiak, A., and West, S.C. (1998). Visualisation of human rad52 protein and its complexes with hRad51 and DNA. J. Mol. Biol. *284*, 1027–1038.

Yamaguchi-Iwai, Y., Sonoda, E., Buerstedde, J.M., Bezzubova, O., Morrison, C., Takata, M., Shinohara, A., and Takeda, S. (1998). Homologous recombination, but not DNA repair, is reduced in vertebrate cells deficient in RAD52. Mol. Cell. Biol. *18*, 6430–6435.

Zan, H., Tat, C., Qiu, Z., Taylor, J.R., Guerrero, J.A., Shen, T., and Casali, P. (2017). Rad52 competes with Ku70/Ku86 for binding to S-region DSB ends to modulate antibody class-switch DNA recombination. Nat. Commun. *8*, 14244.

Cell Reports, Volume *18*

Supplemental Information

Human RAD52 Captures and Holds DNA Strands, Increases DNA Flexibility, and Prevents Melting of Duplex DNA: Implications for DNA Recombination

Ineke Brouwer, Hongshan Zhang, Andrea Candelli, Davide Normanno, Erwin J.G. Peterman, Gijs J.L. Wuite, and Mauro Modesti

FIGURE S1

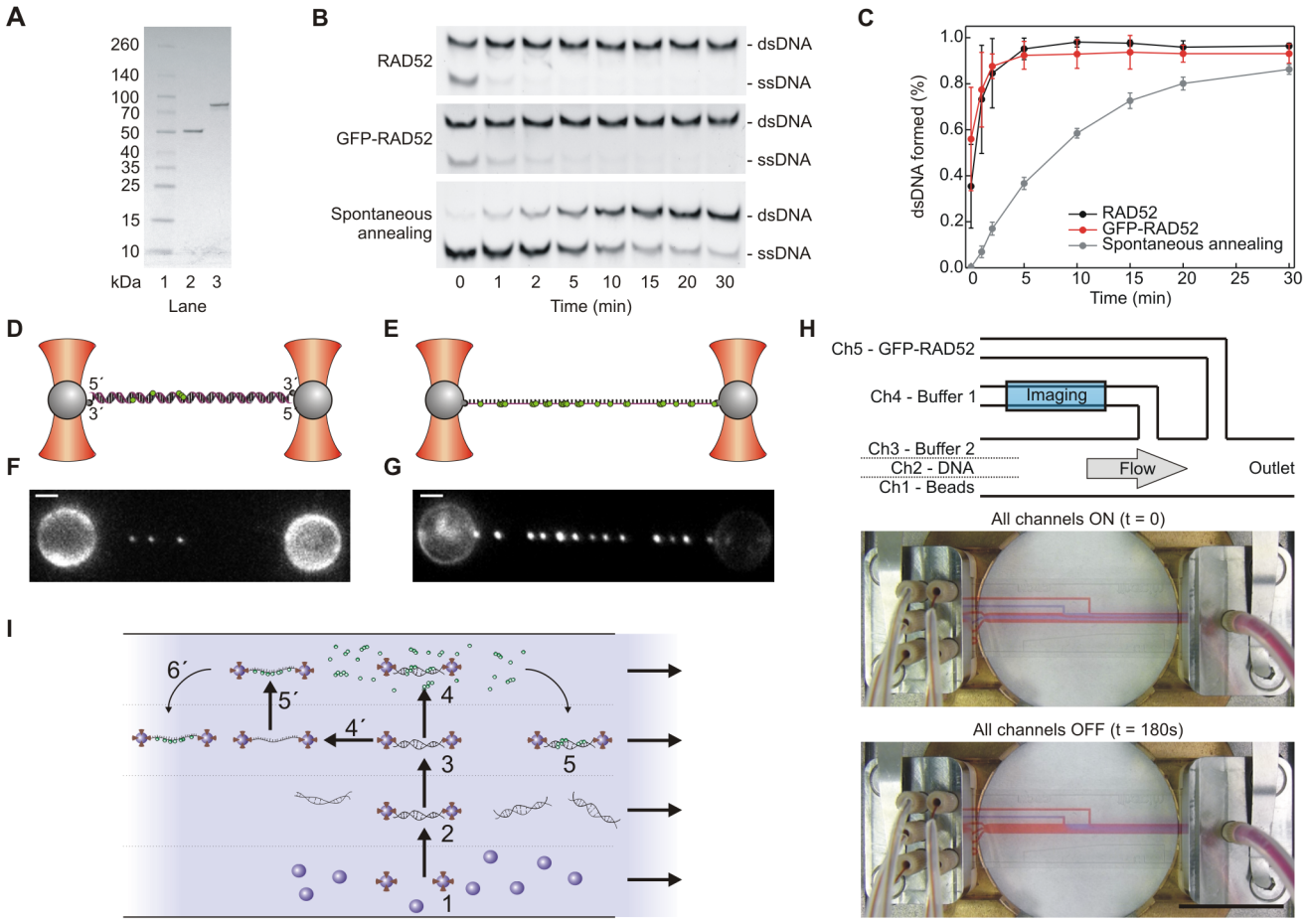

Figure S1. Functionality of GFP-RAD52 and experimental assay, related to Figures 1, 2, 3, and 4.

A) SDS-PAGE and Coomassie Blue staining analysis of purified wild-type RAD52 and N-terminally tagged GFP-RAD52. Lane 1: molecular size marker. Lanes 2 and 3: 0.5 µg of RAD52 and GFP-RAD52, respectively.
B) Kinetics of single-strand annealing reactions mediated by RAD52, eGFP-RAD52 or in the absence of protein using a FAM-labeled 50-mer oligonucleotide and its unlabeled complementary strand as described below in Supplemental Experimental Procedures. Progressive annealing was detected by taking samples at different time points. After fractionation of the samples by native PAGE, fluorescence signal was collected using a CCD camera.
C) Quantification of annealing activities detected as in (B). The extent of annealing is assessed as the percentage of dsDNA formed over time for RAD52 (black dataset), GFP-RAD52 (red dataset), and spontaneous annealing in the absence of protein (grey dataset). Error bars: standard error of the mean (SEM) from four independent experiments.
D) Schematic of a dsDNA molecule (purple) tethered between two optically trapped micrometer-sized polystyrene beads (grey) with GFP-RAD52 complexes (green) bound to the dsDNA molecule. By manipulating the position of the beads the extension of the DNA molecule can be controlled while the tension in the molecule is monitored. At the same time, the proteins can be directly visualized with single-fluorophore resolution using wide-field fluorescence microscopy.
E) Schematic, such as shown in (D), but for GFP-RAD52 complexes bound to ssDNA complex.
F) Typical fluorescence image emitted by GFP-RAD52 complexes bound to dsDNA such as schematically shown in (D). Scale bar: 2 µm.
G) Typical fluorescence image emitted by GFP-RAD52 complexes bound to ssDNA such as schematically shown in (E). Scale bar: 2 µm.

H) Schematic of the 5-channel flow cell used (top panel), indicating the solutions in the different channels. For the dsDNA binding experiments, the solutions in the channels were as follows: channel 1, beads; channel 2, DNA; channels 3 and 4, experiment buffer (buffers indicated in the text/captions of the manuscript); and channel 5, GFP-RAD52 solution. For the ssDNA experiments, they were as follows: channel 1, beads; channel 2, DNA; channel 3, melting buffer (20 mM Tris-HCl pH 7.6); channel 4, experiment buffer (buffers indicated in the text/captions of the manuscript; and channel 5, GFP-RAD52 solution. The imaging experiments were done deep into channel 4 (blue rectangle: "Imaging") after stopping the flow in all channels. The mixing there is very slow (longer than the timescale of the experiments). As can be seen using red and blue colored aqueous solutions, when all channels are flowing (middle panel) the fluids in the 5 channels do not mix. Next, channels 1 and 2 were closed, and after 30 s of flow all channels were closed. 180 s after stopping the flow there is no mixing deep into channel 4 in the imaging area (bottom panel). Scale bar: 2 cm.
I) Schematic explaining the imaging assays. A typical experiment comprises the following steps: step 1, capture of 2 beads; step 2, capture of a single dsDNA-molecule between these beads; step 3, probing the mechanical properties of the tethered dsDNA molecule, to ensure that it is a single molecule with the expected mechanical properties; then either step 4, the dsDNA is incubated in a channel with the GFP-RAD52 and step 5 the construct is brought back to the buffer channel where it can be imaged in the absence of fluorescence protein in the background; or step 4', the tension on the dsDNA molecule is increased to generate an ssDNA molecule by force-induced melting; step 5', the ssDNA is incubated in the protein channel; and step 6', the construct is brought into the buffer channel for imaging. Imaging of the GFP-RAD52 complexes bound to DNA was always performed in the absence of flow as indicated in panel (H).

FIGURE S2

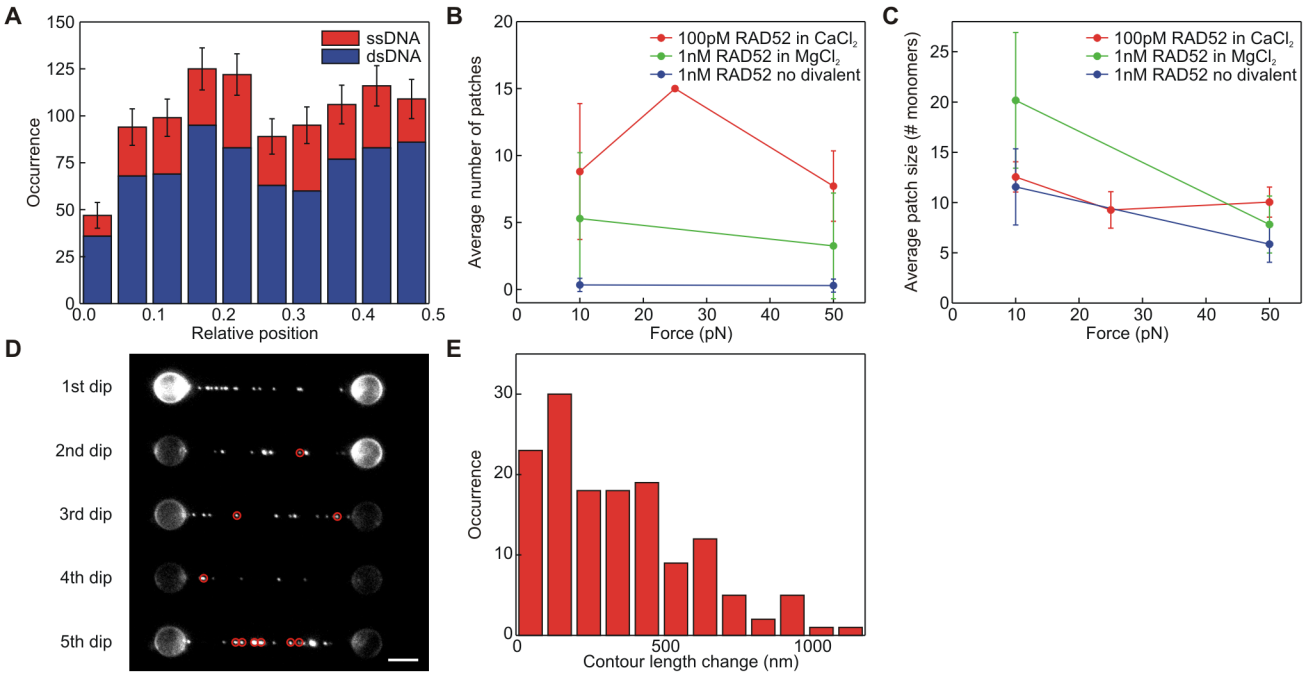

Figure S2. GFP-RAD52 binding to ssDNA, related to Figure 1.

A) Relative position along the DNA of all detected GFP-RAD52 complexes on ssDNA (red, N = 282) and on dsDNA (blue, N = 720). Because the orientation of the DNA molecule between the two beads is unknown in the experiments, the distance to the closest bead was used as a measure for the position. Error bars: statistical errors in the number of counts.
B) Relation between the average number of patches and the force on ssDNA at the indicated GFP-RAD52 concentrations and given cationic conditions.
C) Relation between the average patch size and the force on ssDNA at the indicated GFP-RAD52 concentrations and given cationic conditions. In contrast to what was observed on dsDNA (Figure 2C), GFP-RAD52 patch size on ssDNA is independent of force. Error bars: SEM.
D) For the ssDNA molecule shown in the figure, the probability of a new RAD52 patch to bind to a location of a previously bound one is on average 7.5 ± 3 % (SEM) over the 5 subsequent 2 s-long dipping. Globally, we observed 21 co-localizing patches over the 144 detected patches on 8 different ssDNA constructs with an overall average patch grow probability of about 14 ± 4 % (SEM). Scale bar: 5 µm.
E) Histogram of contour length changes observed in the rupture events for ssDNA. Data were generated by applying a step-fitting algorithm (Kerssemakers et al., 2006) to the traces such as the red curve shown in Figure 1D. On average, the contour length changes in step of 0.35 ± 0.02 µm (SEM, N = 143).

FIGURE S3

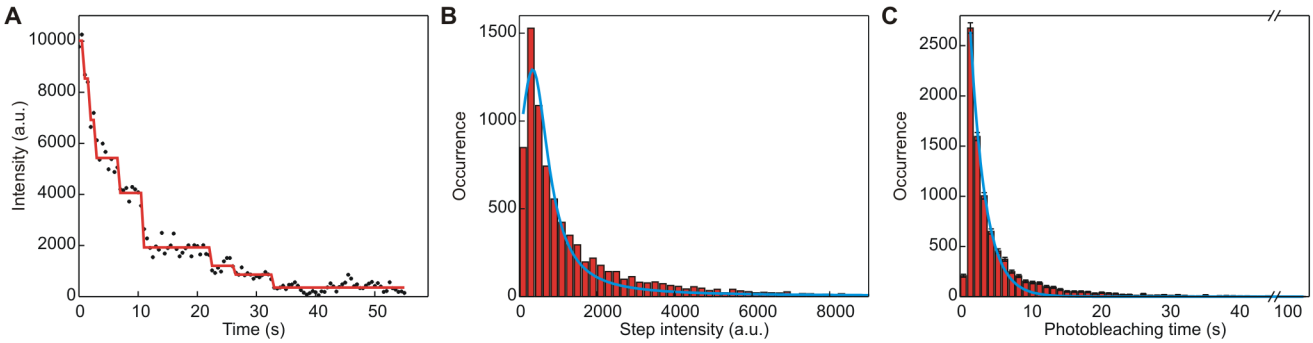

Figure S3. Intensity calibration and bleaching time of individual GFP-RAD52 proteins, related to Figures 1 and 2.

A) Example of fluorescence intensity trace of an individual GFP-RAD52 complex as a function of time. Step values were obtained from such traces using a step fitting algorithm (Kerssemakers et al., 2006).
B) Histogram of step intensities (N = 8188). Lorentzian fit (blue curve) was used to determine the most likely value giving 345 ± 10 intensity a.u., which we assume as the average intensity value of a single GFP.
C) Histogram of photobleaching times from the dataset shown in (B). The bleaching time obtained from an exponential fit (blue curve) to the data is 2.17 ± 0.03 s. Error bars: statistical errors in the number of counts.

FIGURE S4

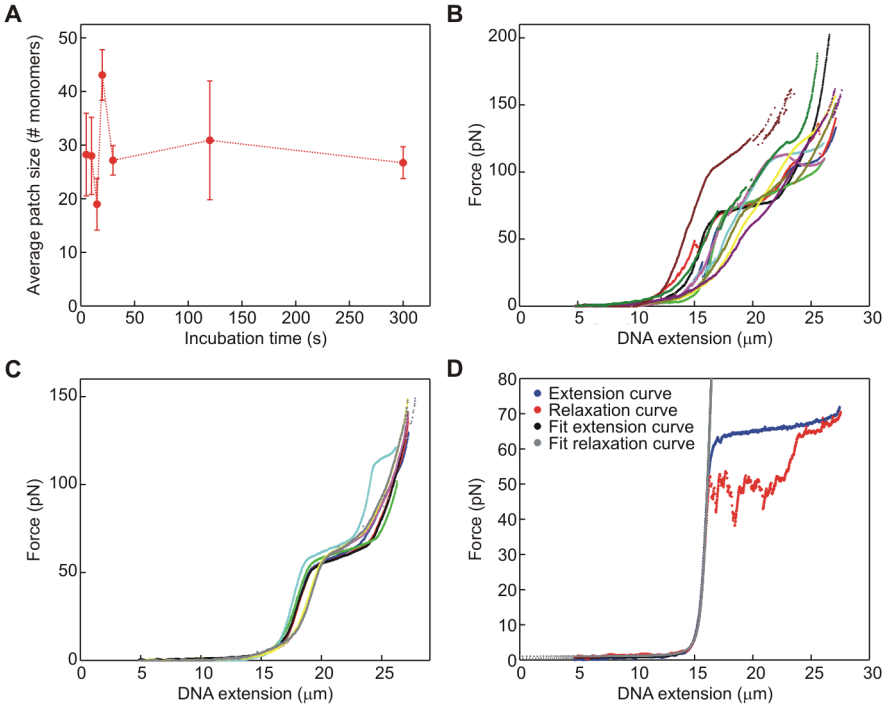

Figure S4. GFP-RAD52 binding to dsDNA, related to Figure 2 and Table 1.

A) Average patch size as a function of the incubation time, shown for the data measured on dsDNA at a GFP-RAD52 concentration of 20 nM, in the presence of $CaCl_2$ and with a DNA tension of 50 pN. For the other conditions, similar results were obtained. Data display no dependence of the patch size on the incubation time, showing no evidence for a mechanism of cooperative patch growth. Error bars: SEM.
B) Force-extension curves of 11 different GFP-RAD52-dsDNA complexes shows irregular force-extension behavior, caused by nonspecific sticking of DNA-bound RAD52 to the beads. This made it impossible to obtain reliable eWLC fits to this data. Nevertheless, the data do not show the typical plateau at around 65 pN indicating the melting of the duplex DNA. Instead the curves show a continuous raise of the force during extension.
C) Force-relaxation curves of 8 different GFP-RAD52-dsDNA complexes. These curves are more regular and reliable eWLC fits can be performed on them. Fit parameters are reported in Table 1.
D) Example of force-extension data recorded during a stretching-relaxation cycle in the absence of GFP-RAD52. Blue curve shows extension curve and red curve relaxation data. Up to 30 pN, the curves are well described by a fit to the eWLC model. Fits are shown in light grey (extension data) and dark grey (relaxation data). Fit parameters for extension and relaxation are reported in Table 1.

FIGURE S5

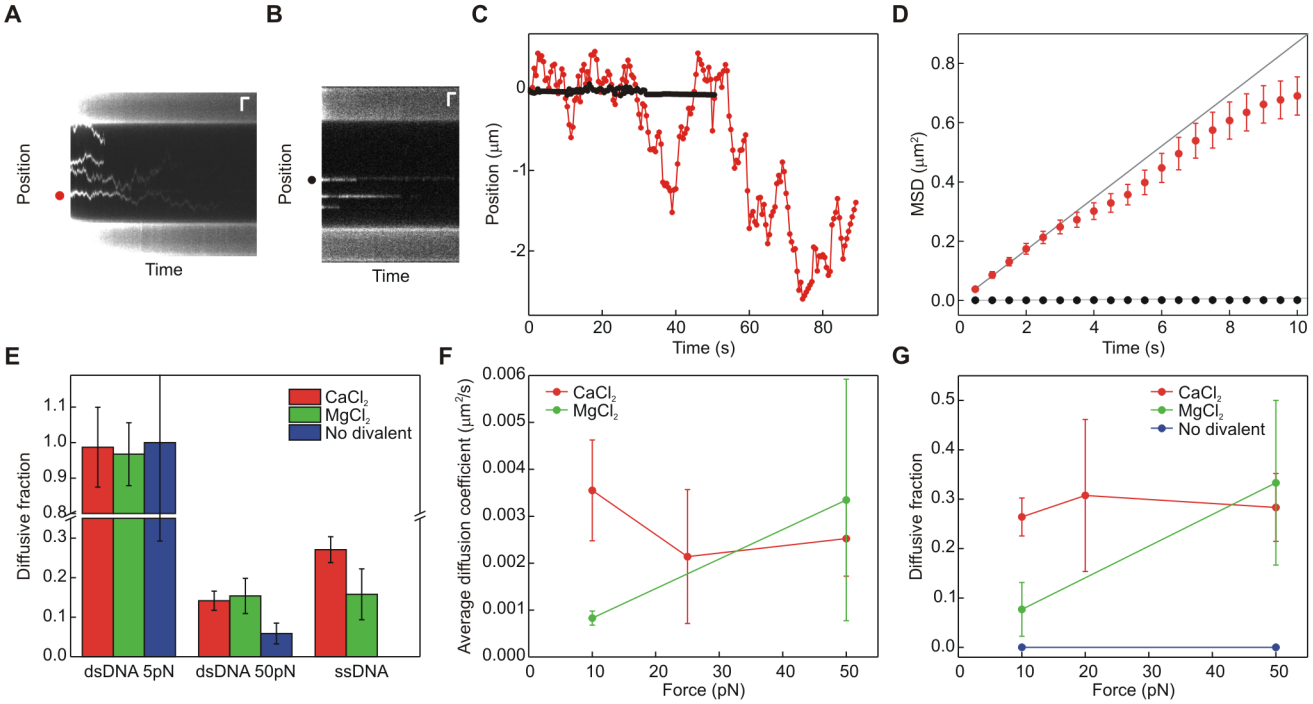

Figure S5. Analysis of GFP-RAD52 diffusion, related to Figures 1, 2, and 3.

A) Typical example of a kymograph of diffusive GFP-RAD52 particles. Data were recorded at 20 nM GFP-RAD52 in the presence of $CaCl_2$ on dsDNA with a tension of 5 pN. Scale bars: 2 µm, 10 s.
B) Typical example of a kymograph of static GFP-RAD52 particles. Data were recorded at 20 nM GFP-RAD52 in the presence of $MgCl_2$ on dsDNA with a tension of 50 pN. Scale bars: 2 µm, 10 s.
C) Displacement from the initial position for a mobile particle (red dataset, corresponding to the particle indicated by the red dot in (A)) and static particle (black dataset, corresponding to the particle indicated by the black dot in (B)).
D) Mean-squared displacement analysis of the particles in (C). Linear fits to the first 5 points of the MSD reveal a diffusion coefficient of $(4.4 \cdot 10^4)$ nm^2/s (red dataset) and 91 nm^2/s (black dataset). Error bars: SEM.
E) GFP-RAD52 diffusive fraction as a function of cationic conditions for dsDNA at different forces and for ssDNA. Error bars: statistical errors in the number of counts.
F) Effect of the tension on ssDNA constructs on the diffusion coefficients of GFP-RAD52 complexes in $CaCl_2$ or $MgCl_2$.
G) Effect of the tension on ssDNA constructs on the diffusive fraction of GFP-RAD52 complexes in $CaCl_2$, $MgCl_2$ or without divalent cation.

SUPPLEMENTAL EXPERIMENTAL PROCEDURES

Proteins purification

Plasmid pET28a-eGFP-polyHis-hRAD52 for the expression of N-terminally tag GFP-RAD52 was constructed by modification of pET28a-polyHis-hRAD52 (de Jager et al., 2001). RAD52 and GFP-RAD52 expression was performed in Rosetta(DE3)pLysS cells (Novagen) grown in LB medium containing kanamycin at 25 µg/ml and chloramphenicol at 34 µg/ml. Two liters of the same medium was inoculated with 20 ml of a saturated overnight pre-culture and incubated at 37°C with shaking. Expression was induced with 0.5 mM IPTG when the optical density at 600 nm reached 0.5. After overnight growth at 16°C, the cells were harvested by centrifugation (4,500 × g, 15 min, 4°C), resuspended with 15 ml PBS and stored at -20°C. The cell paste was thawed and mixed with one volume of lysis buffer (40 mM Tris-HCl pH 7.5, 1600 mM NaCl, 4 mM 2-Mercaptoethanol, 20 mM Imidazole, 10 % glycerol) supplemented with 1 tablet of protease inhibitors without EDTA (Pierce), 1 mM PMSF, 10 mg lysozyme and 1 ml of 10 % Triton X-100. After resuspension the lysate was treated by sonication to reduce the viscosity. The lysate was clarified by centrifugation (25,000 × g, 60 min, 4°C). The supernatant was collected and passed through a 5 ml HisTrap FF Crude column (GE Healthcare) equilibrated with 20 mM Tris-HCl pH 7.5, 800 mM NaCl, 2 mM 2-Mercaptoethanol, 10 mM Imidazole and 10 % glycerol. The column was washed extensively with 20 column volumes of the same buffer and proteins were eluted with 25 ml of the same buffer but containing 300 mM NaCl. The eluate was dialyzed against 2 liters of 20 mM Tris-HCl pH 8.0, 50 mM KCl, 1 mM EDTA, 1 mM DTT, and 10 % glycerol overnight at 4°C and applied to a 5 ml Heparin column (GE Healthcare) equilibrated with the dialysis buffer, washed by raising the salt to 100 mM and eluted with 0.1–1 M KCl gradient. The peaks of RAD52 and GFP-RAD52 eluting around 300 mM KCl (Figure S1A), were collected, divided in aliquots and flash frozen in liquid nitrogen before storage at -80°C.

Annealing assay

Two complementary 50-mer oligonucleotides, oligo 1 (5'-TAA ATG CCA ATG CTG CTG ATA CGT ACT CGG ACT GAT TCG GAA CTG TAA CG-3'), and oligo 2 (5'-CGT TAC AGT TCC GAA TCA GTC CGA GTA CGT ATC AGC AGC ATT GGC ATT TA-3') were purchased from Eurogentec. Oligo 1 was 5'-end labeled with FAM. FAM-labeled oligo 1 (final concentration 10 nM), complementary oligo 2 (10 nM), RAD52 protein (final concentration 100 nM) or GFP-RAD52 (final concentration 100 nM) were added in reaction buffer (final volume 90 µl) containing 0.25 mM DTT, 0.25 mM EDTA, 5 mM Tris-HCl pH 8.0, 40 mM KCl, 2.5 % Glycerol, 50 µg/ml BSA, and 2.5 mM $MgCl_2$, kept at room temperature. At the time indicated, 10 µl of reaction mixture were taken out and quenched by addition of 2 µl of stop buffer containing 5 µM unlabeled oligo 1, 5% SDS, 250 mM EDTA and 2.5 mg/ml proteinase K for 15 min at room temperature. DNA products were fractionated by native polyacrylamide gel electrophoresis using a Tris-Borate buffer system. Fluorescent images (Figure S1B) were acquired using a ChemiDoc MP imaging system (Bio-Rad).

DNA constructs for optical trapping experiments

For optical trapping experiments with both ss and dsDNA, biotinylated DNA constructs based on the 48 517 nt-long λ phage DNA were used in combination with streptavidin-coated beads with a diameter of 4.5 µm (Spherotech). The preparation of the construct for the dsDNA experiments was described previously (van den Broek et al., 2005). In brief, it consists of using Klenow DNA Polymerase in combination with biotin-14-dATP and biotin-14-dCTP to label the 5' overhangs of both strands of the dsDNA. The preparation of the construct which can be used for ssDNA experiments upon force-induced melting was described previously (Candelli et al., 2013). In brief, biotinylation of both the 3' and 5' end of the same DNA strand is achieved by sequential annealing and ligation of oligonucleotides (5'-GGG CGG CGA CCT GGA CAA-3' and 5'-AGG TCG CCG CCC TTT TTT TTT TTT-3') to first biotinylate the 5' end and subsequently the annealing and ligation of an oligonucleotide (5'-TTT TTT TTT TTT AGA GTA CTG TAC GAT CTA GCA TCA ATC TTG TCC-3') to the 3' end of a linearized λ DNA molecule.

Experimental conditions for optical trapping experiments

Catching of the beads and the DNA were performed in PBS buffer (10 mM phosphate, 150 mM NaCl, pH 7.3–7.5). DNA melting for generation of ssDNA templates was performed in 20 mM Tris-HCl pH 7.6. Buffer conditions in the protein and imaging channels were 20 mM Tris-HCl pH 7.6, 100 mM KCl and either 1 mM $MgCl_2$, 1 mM $CaCl_2$, or no divalent cations.

Experimental apparatus combining optical trapping, fluorescence microscopy, and microfluidics

The custom-built instrument was described in detail elsewhere (Gross et al., 2010). Briefly, it is built around a Nikon inverted microscope equipped with a 1064 nm trapping laser, where the two traps which can be manipulated independently using steerable mirrors are generated by splitting the laser into two perpendicularly polarized beams using a half-wave plate

and polarizing beam splitter cube. Using a second polarizing beam splitter, the two trapping beams are recombined and coupled into a water-immersion objective on the microscope. By collecting the transmitted light using an oil-immersion condenser and rejection of the unwanted light by a third polarizing beam splitter, the force can be detected on a position-sensitive diode. The bead-to-bead distance was measured using real time template matching of bright field images obtained by blue LED illumination. For fluorescence imaging, 491 nm and 639 nm excitation lasers were simultaneously coupled into the microscope and imaged on an EMCCD camera. A multichannel laminar flow cell was used to enable fast buffer exchange between beads, DNA, buffer, and protein solutions.

Quantification of fluorescence intensity

To obtain the stoichiometry of the DNA-bound GFP-RAD52 complexes, we applied a step-fitting algorithm (Kerssemakers et al., 2006) to the photobleaching traces of all individual fluorescent patches and determined the average intensity of a single GFP from a Lorentzian fit to the histogram of step intensities (Figure S3). From this, the total number of eGFP molecules in each patch could be inferred from the initial fluorescence intensity of each patch.

Quantification of protein diffusion

The diffusion of GFP-RAD52 complexes along dsDNA and ssDNA was quantified by tracking the proteins for a large number of frames (on average 29 ± 2 s). The corresponding diffusion coefficient was calculated using 1-dimensional mean square displacement (MSD) analysis (Heller et al., 2014b). Because the pixel size of our camera is 130 nm, we estimate that the minimal diffusion we could observe would be if the particle moves a distance of 1 pixel during the average interaction time. Therefore, we estimate the minimum detectable diffusion of RAD52 interactions using our system to be 583 nm^2/s. We therefore assume that a particle is static if its diffusion coefficient is lower than this value and that it is diffusive when its diffusion coefficient is higher than this value.

Experiments of ssDNA oligonucleotide capture in *trans* by RAD52

The sequence of the 60-mer fluorescent oligonucleotide was Atto647N-5'-ACA-GCC-AGA-CCC-GGA-CGC-TGA-CGC-TCG-ACC-GTG-AAA-TCA-CGC-TGC-CAT-CCT-CCG-GTA-CCG-3'. Experiments were performed in a flow cell with six channels. DNA molecules with GFP-RAD52 bound were incubated for 30 s in a 10 nM solution of the oligonucleotides in 20 mM Tris-HCl pH 7.6, 100 mM KCl and 1 mM $CaCl_2$ and visualized in the same buffer in the absence of oligonucleotides in solution.

SUPPLEMENTAL REFERENCES

van den Broek, B., Noom, M.C., and Wuite, G.J.L. (2005). DNA-tension dependence of restriction enzyme activity reveals mechanochemical properties of the reaction pathway. Nucleic Acids Res. *33*, 2676–2684.

de Jager, M., Dronkert, M.L., Modesti, M., Beerens, C.E., Kanaar, R., and van Gent, D.C. (2001). DNA-binding and strand-annealing activities of human Mre11: implications for its roles in DNA double-strand break repair pathways. Nucleic Acids Res. *29*, 1317–1325.